XoveTIC: Impulsando el talento científico

Editorial Office

Servizo de Publicacións (SPU)
Universidade da Coruña
Maestranza 9, 15001 A Coruña, Spain

Handle: 2183/40661
DOI: 10.17979/spudc.9788497498913

Cover image courtesy of CITIC—Research Center of Information and Communication Technologies, University of A Coruna, Spain
CITIC, as a center accredited for excellence within the Galician University System and a member of the CIGUS Network, receives subsidies from the Department of Education, Science, Universities, and Vocational Training of the Xunta de Galicia. Additionally, it is co-financed by the EU through the FEDER Galicia 2021-27 operational program (Ref. ED431G 2023/01)

Proceedings XoveTIC 2024. Impulsando el talento científico.

This volume was typeset in LaTeX by the editors using *varianTeX* — a reusable template for journals in the Humanities, developed by Wout Dillen. *varianTeX* is open source, available on GitHub, and deposited in the Zenodo Open Science Repository. DOI: 10.5281/zenodo.3484651.

Segmentation of the Bone Structure from MRI Knee Joint - A Use Case

Vasco Silva, Adélio Vilaça, Rita Veloso, Luís Coelho, and Renato Magalhães

ISEP, Polytechnic of Porto, Rua Dr. António Bernardino de Almeida, 4249-015 Porto, Portugal
CAC ICBAS-CHP { Centro Académico Clínico Instituto de Ciências Biomédicas Abel Salazar { Centro Hospitalar Universitário de Santo António, Porto, Portugal
Executive Board Member, Centro Hospitalar Universitário Santo António, Porto, Portugal
LabRP-CIR, ESS, Polytechnic of Porto, Rua Dr. António Bernardino de Almeida, 4200-072 Porto, Portugal
Correspondence: rfm@ess.ipp.pt

DOI: *https://doi.org/10.17979/spudc.9788497498913.12*

Abstract: Manual and automatic segmentation techniques can be applied to DICOM medical images from magnetic resonance imaging (MRI) to extract certain structures, such as soft tissues, but the precise extraction of bone structures may be limited. This study studies these types of knee bone tissue segmentation on MRI, to avoid the need to resort to computed tomography (CT) for obtaining the desired bone structures. Manual segmentation was done using ITK-Snap and automatic segmentation algorithms were applied in Python and the ITK library. As a result of this study, it was found that although manual segmentation allowed for precise and consistent identification of the femur, tibia, fibula, and patella, the automatic segmentation needed to achieve the same level of accuracy.

Introduction

The advancement of automatic segmentation in medical imaging has revolutionized diagnostics and treatment. Traditional methods like X-rays, CT scans, and MRIs can be time-consuming and prone to human error. Automatic segmentation, utilizing advanced algorithms and AI, optimizes repetitive tasks, enhancing efficiency and diagnostic accuracy (Gobert Lee, 2020). These tools improve workflow speed, image interpretation precision, and support early pathology detection and surgical planning, allowing healthcare professionals to focus on complex tasks and personalized care (Gobert Lee, 2020).

MRI, or magnetic resonance imaging, visualizes internal body structures without ionizing radiation. Developed by Nobel laureates Paul Lauterbur and Peter Mansfield (NobelPrize.org, 2024), MRI uses the behavior of hydrogen nuclei in body tissues, which align under a strong magnetic field. A radiofrequency pulse deflects them, and they release energy as they realign, which is processed into detailed images. T1 and T2 relaxation times, varying by tissue type, determine signal intensity (M. A., 2014; Marques et al., 2019).

T1 and T2 weighted sequences are crucial for obtaining MRI images, as each highlights different tissue characteristics. Along with Proton Density (PD) sequences, they are essential for characterizing various pathologies

(Mafraji, 2023; Marques et al., 2019). Table 1 summarizes the main characteristics and applications of these techniques.

Table 1: Physical Principles and Clinical Applications of T1, T2, and PD Sequences in MRI

Sequences	Physical Principles	Clinical Applications
T1	Measures the longitudinal relaxation time (T1) following the application of a radiofrequency pulse (Mafraji, 2023).	Provides detailed anatomical images, primarily highlighting structures such as fat, which appears bright (high signal intensity), while water and fluids appear relatively dark (low signal intensity) (Mafraji, 2023).
T2	Measures the transverse relaxation time (T2), sensitive to the water and fluid content within tissues (Mafraji, 2023).	More sensitive to the presence of fluids and inflammation, making it useful for detecting oedema and inflammatory processes. Water and fluids appear bright, while fat appears relatively dark (Mafraji, 2023).
PD	Utilises a long repetition time to reduce T1 effects and a short echo time to minimise T2 effects (Marques et al., 2019).	Used in the diagnosis of joint diseases and injuries, such as meniscal tears and conditions with high proton density (Marques et al., 2019).

Despite advancements in medical imaging, challenges remain, such as ionizing radiation exposure in CT scans and the risk of adverse reactions to contrast agents. CT is typically used for automatic bone segmentation due to its high spatial resolution, but it poses health risks. MRI, while better for soft tissue visualization, struggles with 3D bone reconstruction. Additionally, many hospital PACS lack tools for bone segmentation from MRI. This study proposes an automatic solution for knee bone reconstruction from MRI DICOM images, improving diagnosis without the risks of CT scans (Decazes et al., 2021; M. A., 2014; MRIMaster, 2024).

Methods

Two sets of knee MRI scans, RM_31 and RM_164, were evaluated. The T1 sequence in the sagittal plane was selected for its superior fluid contrast, featuring short repetition times (300-600 ms) and reduced echo times (10-15 ms). The RM_164 series was acquired under similar conditions but with finer slices between the planes. Detailed characteristics are provided in Table 2 (MRIMaster, 2024).

Table 2: Information from MRI RM_31 and RM_164

Images	Dimensions (i, j, k)	Pixel spacing (x, y, z)	Intensity
RM_31	384 x 384 x 31	0.3906 x 0.3906 x 3.3000	0 - 3070
RM_164	512 x 512 x 164	0.3711 x 0.3711 x 0.8	0 - 3216

After learning about the knee's anatomy and identifying structures in MRI images, RM_31 was chosen as the focus for both manual and automatic segmentations. The manual segmenta-

tion was performed using ITKSnap software, version 4.0.1 for macOS, with labels assigned to each bone of the knee. Additional details can be found in Table 3 (ITK-SNAP, 2023).

Table 3: Description and characteristics of the tags used for segmentation

Labels	Pixel Value	Colour
Clear Label	0	
Femur	1	
Tibia	2	
Fibula	3	
Patella	4	

All Python code was developed using the ITK library in Visual Studio Code, providing tools for reading, processing, segmenting, and registering medical images in 2D or 3D. The *DICOM-toVTK.py* algorithm converts DICOM images to VTK format for compatibility with ITKSnap for anatomical segmentation. This library extracts key statistics such as centroid, mean, median, standard deviation, and pixel value ranges for each structure. Additionally, specific distances like the inter-epicondylar femur distance and mediolateral tibial distance were calculated to compare manual and automatic segmentations, as shown in Figure 1 (Gali et al., 2015; Tabary et al., 2020).

Figure 1: Calculated distances: A – inter-epicondylar distance of the femur, B - mediolateral distance of the superior tibial articular surface, C - sagittal diagonal distance of the fibula and D - distance between the superior and inferior poles of the patella

Analyzing MRI characteristics is essential for identifying limitations in automatic segmentation and selecting suitable tools. A semi-automatic algorithm was developed to manually mark seeds on four bones, aiding region-growing segmentation. Though not fully automatic, it is practical and efficient. A median filter was applied to smooth images and enhance bone distinction. Effective filters included Connected Threshold, Confidence Connected, and Neighborhood Connected, while
itk.RegionGrowImageFilter was discarded. The Otsu filter and mask converted images to binary format, improving region growth. These enhancements were tested on RM_31, with Figures 2 and 3 illustrating the feature pipelines and automatic segmentation algorithms developed (ITK, 2024; McCormick et al., 2014; VTK, 2024).

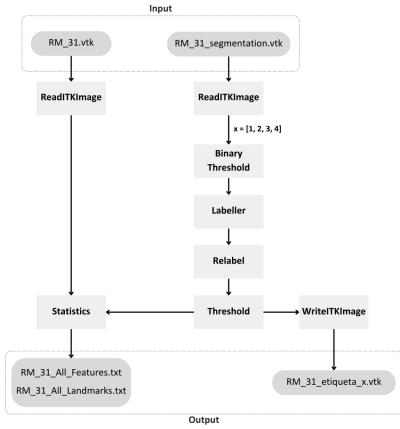

Figure 2: Pipeline for acquiring features and landmarks of each structure labelled in the RM_31 image segmentation

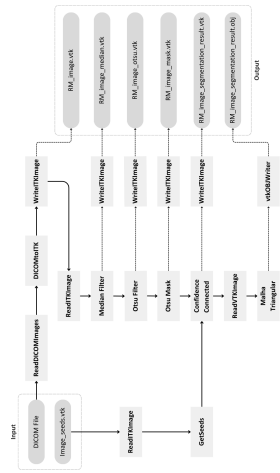

Figure 3: Automatic/semi-automatic segmentation algorithm pipeline

Results

After converting the RM_31 image to VTK format for visualization in ITK-Snap, manual segmentation of the bony structures of the knee was performed using this application, resulting in Figure 4.

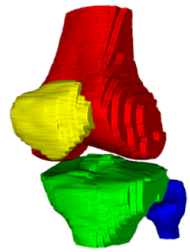

Figure 4: Manual segmentation of the four knee bone structures from MRI RM_31

Through the execution of algorithms to acquire the characteristics of each segmented structure. Results were extracted and the Table 4 details the attributes of the pixel values associated with each bone.

Table 4: Characteristics of pixel intensities for each segmented region

Structure	Mean	Median	Std. Deviation	Min.Pixel Value	Max.Pixel Value
Femur	1300	1360	240.687	12	2039
Tibia	985	1010	207.537	18	1923
Fibula	983	1018	185.553	289	1451
Patella	1075	1121	289.552	99	1909

MRI data lack a defined mean or median for pixel values in bone tissue, unlike CT, which has a distinct range. While the tibia and fibula show no significant MRI intensity differences,

the tibia and femur do. Minimum and maximum pixel values suggest that a range between 1100 and 1600 could be useful for future region-growing, though avoiding extremes is crucial to prevent errors. Table 5 shows the centroids of segmented structures in voxel and real-world coordinates, aiding in morphological analysis.

Table 5: Centroids of segmented structures, ijk voxel coordinates and xyz real coordinates

Centroid	i	j	k	x (mm)	y (mm)	z (mm)
Femur	175	145	14	234.81	-82.99	120.32
Tibia	218	309	14	251.45	-18.82	120.95
Fibula	293	330	4	280.59	-10.78	86.67
Patella	63	184	13	191.02	-67.61	118.62

Morphological statistics, like volumes and distances, were obtained to compare with upcoming automatic segmentation results. The femur and tibia had the largest manually obtained volumes (225,018.937 mm^3 and 138,433.219 mm^3, respectively). Both bones showed similar mediolateral epiphyseal distances, indicating precise manual segmentation. A comparative study with other segmentations would validate these findings. Subsequently, automatic segmentation was applied, beginning with the median filter, as illustrated in Figure 5.

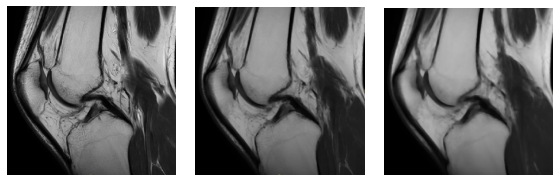

(a) (b) (c)

Figure 5: Application of median filter to RM_31 MRI (a) of radius 1 (b) and 2 (c)

The median filter has clear benefits. With a radius of 1, the image shows significant homogenization, reducing "pixelation." At a radius of 2, tissue boundaries are preserved, with enhanced smoothing, reducing the discrepancy between pixel values, benefiting subsequent algorithms. Region-growing tests on the filtered image show a higher success rate compared to the original, where value ranges are less defined, as seen in Table 4. To ensure consistency, all results used the same starting point: a seed marked in slice 17 of the axial image, specifically in the femur, as shown in Figure 6.

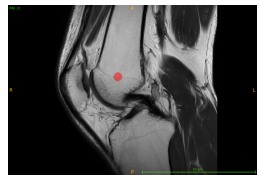

Figure 6: Marking of the seed on the femur in plane 17 of the axial axis of the image RM_31

This procedure illustrates how a healthcare professional can obtain a three dimensional image by placing a seed on a sagittal plane, defining the starting point for subsequent computational algorithms. The size of the marked sample can impact the results, making this reference

point crucial for initial interactions with the image and generating essential data for algorithm development. The Neighborhood Connected algorithm outperformed other tested methods by combining a pixel range with phased neighborhood analysis for segmentation. While it addresses issues with the Connected Threshold method, it has limitations in defining boundaries with neighboring tissues. The Confidence Connected algorithm was selected for its more consistent representation of knee bone anatomy. Additionally, the Otsu Threshold filter optimized segmentation by creating a mask over the image smoothed by the median filter. The results of this process are illustrated in Figure 7 (ITK, 2024).

(a) (b) (c)

Figure 7: Application, in the Median Filter of the RM_31 image (a), of the Otsu Threshold Filter (b) to generate a mask without the pixels with value 1 found (c)

The algorithm emphasized relevant structures by removing unnecessary information. After applying median and Otsu Threshold filters, the region-growing function was used to mark the structures with appropriate labels as shown in Figure 8. 8.

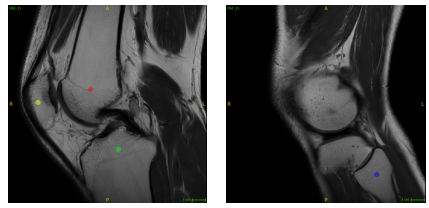

(a) (b)

Figure 8: Marking of the seeds of the femur, tibia and patella in plane 17 and fibula in plane 4 of MRI RM_31

The algorithm developed for the marked seeds, and the MRI RM_31 resulted in the segmentations as shown in Figure 9.

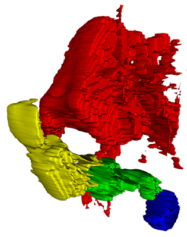

Figure 9: Semi-automatic segmentation result on image RM_31

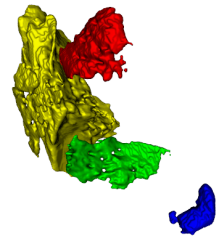

Figure 10: Semi-automatic segmentation result on image RM_164

Both manual and automatic segmentations of the RM_31 images were conducted, and it was

observed that there were significant differences between the two methods. The automatic segmentation method produced unsatisfactory results. The segmentation of the femur was similar to previous results, with some extensions to adjacent structures. In the case of the patella, its segmentation overlapped with underlying tissue, likely due to its proximity and shape. The segmentation of the tibia only captured the spongy bone of its epiphysis due to seed positioning and bone density. The segmentation of the fibula was minimally acceptable, mainly because of its clear separation in the MRI. Following manual optimization of the seed positions, the best result for the same algorithm applied on RM_164 image is shown in Figure 10. These results confirm a recurring challenge: similar pixel intensities in MRI affect segmentation. The region-growing algorithm required the identification of optimal parameters for an accurate representation of knee bones, but this did not ensure consistency across different scans. In the RM_164 image, no structures were identifiable. Additionally, findings were represented in 3D using mixed reality with Hololens 2 to showcase manually segmented structures. The images were exported to OBJ format and converted to lower-resolution surfaces for easier interpretation by healthcare professionals (Kashish and Ghodele, 2020; Microsoft, 2024).

Conclusions

The use of automatic segmentation techniques for representing the bone structure of the knee in MRI images has revealed challenges and opportunities for improvement. Although full automation has not yet been achieved, results indicate that minor improvements are possible with the right functions and tools, suggesting that future adjustments could significantly enhance segmentation. The incorporation of technologies such as extended reality highlights their potential applications in clinical contexts, such as surgical preparation and planning. Future work could benefit from advanced approaches like artificial intelligence and machine learning, which may refine results and enhance clinical application. Overall, a multidisciplinary approach that combines technological development with medical needs is essential for overcoming challenges and providing effective solutions in medical imaging and computer-assisted diagnosis.

Bibliography

P. Decazes, P. Hinault, O. Veresezan, S. Thureau, P. Gouel, and P. Vera. Trimodality pet/ct/mri and radiotherapy: A mini-review, 2 2021.

J. C. Gali, P. Esquerdo, M. A. P. Almagro, and P. A. C. da Silva. Estudo radiográfico da inserção tibial do ligamento cruzado posterior. *Revista Brasileira de Ortopedia*, 50:342–347, 5 2015.

H. F. Gobert Lee. *Deep Learning in Medical Image Analysis*, volume 1213. Springer International Publishing, 2020. ISBN 978-3-030-33127-6.

ITK. Itk - region growing filters, 2024. URL *https://itk.org/Doxygen/html/group__RegionGrowingSegmentation.html*.

ITK-SNAP. Itk-snap, 2023. URL *http://www.itksnap.org/pmwiki/pmwiki.php?n=Main.HomePage*.

S. A. Kashish and N. Ghodele. A review paper on microsoft hololens, 2020. URL *http://www.ijeast.com*.

R. C. B. M. A., Semelka. Mri: Basic principles and applications. *Wiley*, 2014.

M. A. Mafraji. Ressonância magnética, 2023. URL *https://www.msdmanuals.com/pt-pt/profissional/tÃşpicos-especiais/princÃıpios-de-radiologia/ressonÃćncia-magnÃ©tica*.

J. P. Marques, F. F. Simonis, and A. G. Webb. Low-field mri: An mr physics perspective, 6 2019.

M. McCormick, X. Liu, J. Jomier, C. Marion, and L. Ibanez. Itk: enabling reproducible research and open science. *Frontiers in Neuroinformatics*, 8, 2014.

Microsoft. Microsoft hololens 2, 2024. URL *https://www.microsoft.com/pt-pt/hololens/hardware#documente-experiÃłncias*.

MRIMaster. Mrimaster - mri knee, 2024. URL *https://mrimaster.com/plan-knee/*.

NobelPrize.org. The nobel prize in physiology or medicine 1979, 2024. URL *https://www.nobelprize.org/prizes/medicine/1979/summary/*.

M. Tabary, A. Esfahani, M. Nouraie, M. R. Babaei, A. R. Khoshdel, F. Araghi, and M. Shahrezaee. Relation of the chondromalatia patellae to proximal tibial anatomical parameters, assessed with mri. *Radiology and Oncology*, 54:159–167, 4 2020.

VTK. Vtk - overview, 2024. URL *https://vtk.org/about/#overview*.